nature communications

Article

https://doi.org/10.1038/s41467-024-54412-w

Stress-eliminated liquid-phase fabrication of colloidal films above the critical crack thickness

Received: 21 March 2024

Accepted: 10 November 2024

Published online: 02 December 2024

Check for updates

Shiyuan Liu[1,2,8] ✉, Ying Hong[2,8], Wang Hong[3,8], Yi Zheng[2,4,8], Xiaodan Yang[2,4], Xuemu Li[2,4], Zhuomin Zhang[2,4], Xiaodong Yan[2,4], Yao Shan[2], Weikang Lin[2,4], Zehua Peng[5], Xingqi Zhang[6], Xi Yao[7] ✉, Zuankai Wang[5] ✉ & Zhengbao Yang[2] ✉

The thickness of film materials is a critical factor influencing properties such as energy density, optical performance, and mechanical strength. However, the long-standing challenge of the intrinsic thermodynamic limit on maximum thickness often leads to detrimental cracking, compromising these desirable properties. In this study, we present an approach called the stress-eliminated liquid-phase fabrication (SELF) method. The SELF method eliminates the need for substrates to support the precursor solution used for film fabrication. We harness the intrinsic surface tension of the solution by confining it within specifically designed grids in a framework, forming suspended liquid bridges. This technique enables fabrication of crack-free ceramic films within a broad thickness range from 1 to 100 µm. Furthermore, the fabricated PZT films exhibit a high piezoelectric coefficient (d_{33}) of 229 pC N^{-1}. The customizable grids not only offer design freedom for film topologies but also facilitate the fabrication of diverse film arrays without the need for destructive cutting processes. Moreover, the freestanding nature of these films enhances their adaptability for MEMS processing, and the "capillary bridge" topology allows the PZT films to be used in ultrasound focusing transmitter, providing possibilities in the medical imaging.

Colloidal films, characterized by their incorporation of sub-micron dispersed particles, have their performance and applications crucially determined by their thickness. Particularly, thick colloidal films play a pivotal role in modulating photonic crystal pathways, enhancing energy storage efficiency in batteries, and adjusting the mechanical and electrical properties of ceramics[1–6]. However, the conventional method of depositing precursor on a substrate followed by evaporation or sintering presents significant limitations in controlling the quality and thickness of these films[7–9]. When the thickness reaches the so-called critical cracking thickness (CCT), according to Griffith's criterion for crack propagation, further solvent evaporation and increased concentration can cause the stored elastic energy within to exceed a critical threshold, leading to film rupture and failure[3,10–12]. For instance, in piezoelectric ceramic films, this threshold rarely exceeds

[1]Thrust of Smart Manufacturing, System Hub, The Hong Kong University of Science and Technology, Guangzhou, China. [2]Department of Mechanical and Aerospace Engineering, Hong Kong University of Science and Technology, Hong Kong, China. [3]Institute of Advanced Structure Technology, Beijing Institute of Technology, Beijing, China. [4]Department of Mechanical Engineering, City University of Hong Kong, Hong Kong, China. [5]Department of Mechanical Engineering, The Hong Kong Polytechnic University, Hong Kong, China. [6]Department of Engineering - Electrical & Computer Engineering, University of Alberta, Edmonton, AB, Canada. [7]Department of Biomedical Sciences, City University of Hong Kong, Hong Kong, China. [8]These authors contributed equally: Shiyuan Liu, Ying Hong, Wang Hong, Yi Zheng. ✉e-mail: shiyuanl@hkust-gz.edu.cn; xi.yao@cityu.edu.hk; zk.wang@polyu.edu.hk; zbyang@ust.hk

5 μm, posing a challenge in applications such as wearable medical imaging and micro-robotics where piezoelectric materials with thicknesses larger than tens of microns are required[13,14].

Conventional approaches for improving the CCT rely on increasing particle sizes (such as incorporating solid particles into pure liquid-phase colloids) and adding binders, thereby improving the mechanical strength of the films[11,15–17]. Through this approach, the thickness of piezoceramic films can be increased to over 10 μm[18]. However, the introduction of heterogeneous phases inevitably compromises the material properties, resulting in the piezoelectric coefficient d_{33} of thick films being an order of magnitude lower than that of pure-phase thin films or bulk ceramics[19]. Strategies have also been explored to increase CCT by modulating the properties of substrates, while the mismatch of factors such as lattice constants, thermal expansion coefficients, and the hardness between the colloidal film and the substrates will impact the film formation and further complicate the control of CCT[3,10,11]. Additionally, the predominant method for device fabrication has been the top-down thinning of bulk materials to the desired thickness[20]. Yet, when the thickness is reduced to less than 100 μm, the material itself becomes highly susceptible to damage, leading to substantial waste of raw materials.

In contrast to traditional film-substrate coating techniques, we propose a stress-eliminated liquid-phase fabrication (SELF) strategy. Our method leverages capillary forces to suspend pure-phase liquid colloidal films above the substrate, allowing for evaporation, drying, and sintering processes for phase changes without being influenced by tensile stresses (Fig. 1a). This method allows for the large-scale preparation of colloidal film materials of any thickness (including 1 to 100 μm thick PZT films in this work), while maintaining high density and crack-free, without sacrificing their functional characteristics. Leveraging the rapid preparation of piezoelectric thick-film arrays via the SELF method and the inherent concave shape of the resulting ceramic films, we demonstrate their potential applications in conformal devices and ultrasound-focusing transmitters. These advancements highlight application potential in non-invasive medical imaging, tumor ablation, and non-destructive testing.

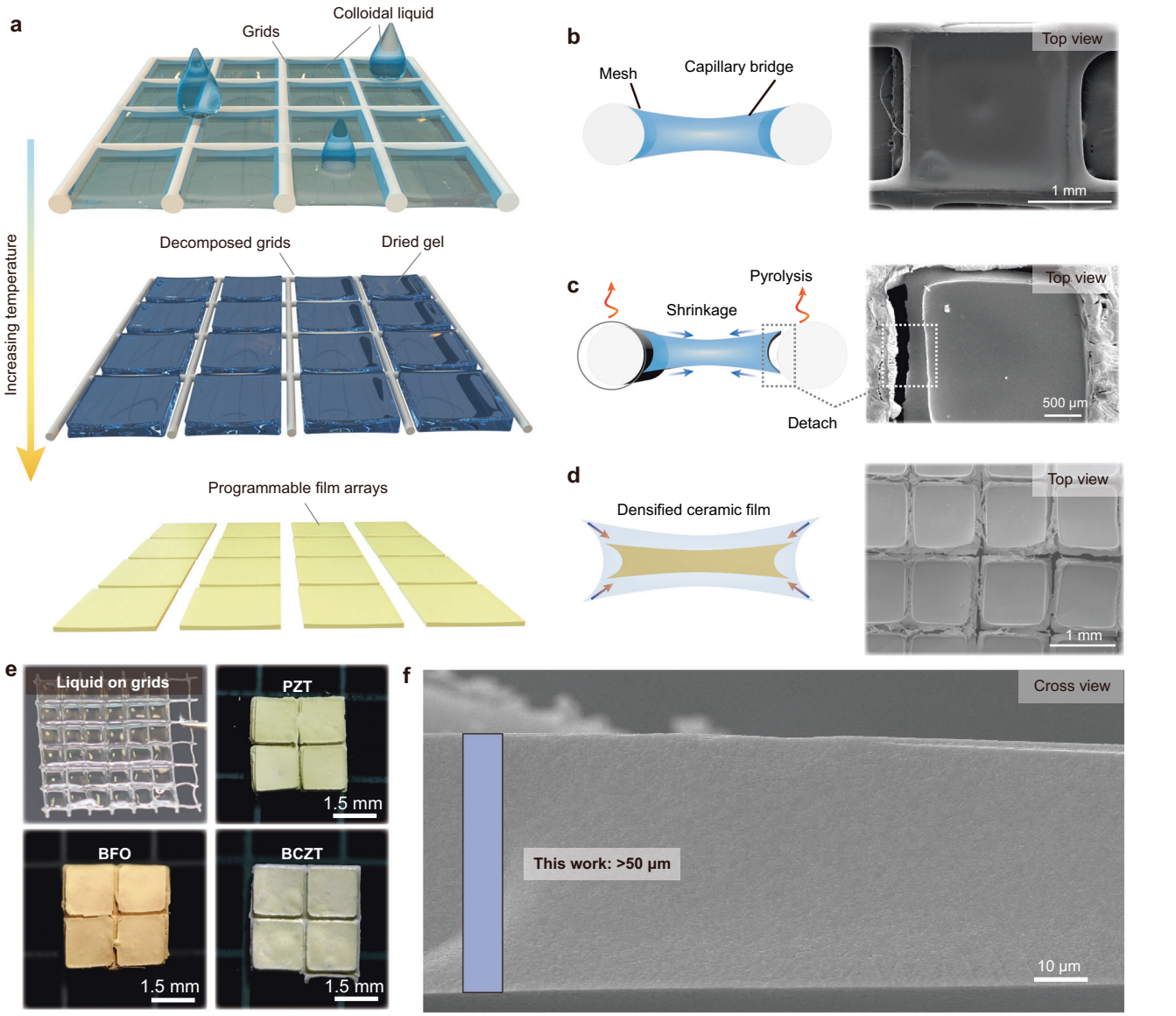

Fig. 1 | The design of the SELF strategy. a The film fabrication route of the SELF strategy. The wetting of artificially designed grids by colloidal precursors. The precursors will dry with air, and the film arrays will be derived after the sintering process. **b** The formation of the colloidal liquid bridge. **c** The detachment during the drying process. **d** The crystallization results. **e** The photograph of the SELF-derived samples, including the liquid on grids, PZT, BFO, and BCZT. **f** The SEM result of the cross-sectional view of the SELF-derived film. The thickness of the film exceeds 50 μm.

https://doi.org/10.1038/s41467-024-54412-w

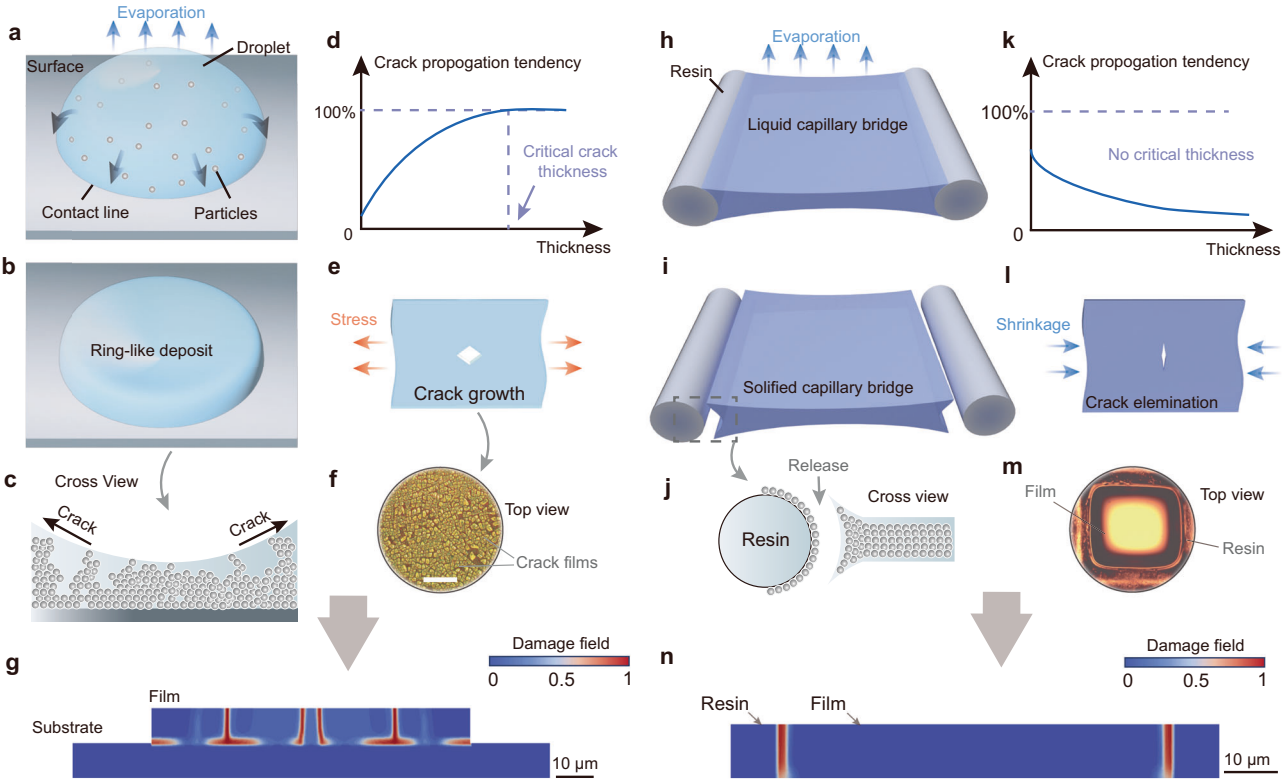

Fig. 2 | Comparison of the stress-eliminated liquid-phase fabrication (SELF) method for preparing crack-free thick colloidal films with the conventional method. a The conventional sol-gel method for ceramic films preparation. The colloidal droplet wets the substrate surface, and the particles migrate toward the edges under Marangoni flows. **b** After evaporation, the droplet forms a "pancake" pattern, where the center is thinner and the edges are thicker. **c** The schematic image of the cross view of the pancake-like deposits. The cracks begin to propagate as the thickness increases. **d** The relationship between the film thickness with the crack propagation tendency. **e** The Griffith's theory of crack propogation model in this case. **f** The optical microscope image of a crack PZT film. The scale bar indicates 400 μm (**g**). The crack propagation simulation results of the conventional film-substrate model. **h** The SELF method for ceramic film preparation. The colloidal liquid forms a capillary bridge in the resin-based grid. **i** The films solify after drying. **j** The edge of the film detaches with the grid. **k** The relationship between the thickness and the crack propagation tendency in the SELF method. **l** The stress distribution and the crack propagation behavior. **m** The optical microscope image of the film in the single grid. The scale bar indicates 400 μm. **n** The crack propagation simulation results of the SELF system. "0" in the damage field indicates undamaged, and "1" indicates fully damaged.

Results

Design and mechanism of the SELF strategy

The SELF strategy requires designing polymer grids and using colloidal precursors. Initially, the colloidal liquid permeates the polymer grid. The grids will confine the colloidal liquid and form complete capillary bridge films, akin to the water film formed on a screen window during rain (Fig. 1b–d). After undergoing a heating and drying process, the colloidal film gradually contracts and solidifies, while the polymer grid decomposes, resulting in the separation of the grid from the film material (Fig. 1c). Through further drying and sintering processes, the films will spontaneously contract and crystallize, yielding large-scale film material arrays. (Fig. 1d). In this work, we fabricate various functional ceramic films, including $PbZr_{0.52}Ti_{0.48}O_3$ (PZT), $BiFeO_3$, and $Ba_{0.85}Ca_{0.15}Zr_{0.2}Ti_{0.3}O_3$. The maximum thickness of the film of PZT reaches 100 μm, which is 10 times larger than the conventional coating methods (Fig. 1e, f).

In the traditional processes employed for the fabrication of colloidal film materials, droplets must first be coated onto the surface of a substrate (Fig. 2a). The droplets initially wet the substrate, with the contact line expanding outwards. When the contact line remains pinned, the evaporation at the edge of the liquid film is enhanced, resulting in a generated capillary flow from within the droplet towards the contact line to compensate for the evaporative losses (Fig. 2a). This flow drives suspended particles toward the edge, culminating in the formation of a pancake-like deposition upon drying, which is known as "coffee-ring effect" (Fig. 2b). This results in a thickness profile characterized by a thin center and a thick edge (Fig. 2c). The tendency of the crack formation during the drying process elevates with the thickness increases. The crack is inevitable when the thickness exceeds a critical value (Fig. 2d). These fissures originate from stress disparities between the film and its substrate. These cracks stem from stress mismatches between the film and its substrate, and the critical crack thickness is influenced by multiple factors, including the differential thermal expansion between the film and substrate, intrinsic stresses developed during sol-to-gel transformation, and the particle size of the film. Overall, due to a competition between the compressive capillary pressure at the top of the colloidal film (colloid-air interface) and the constraint provided by the substrate (colloid-substrate interface), stress accumulation induced by drying occurs within the material. As Griffith developed in 1921, based on the first law of thermodynamics, the minimum stress σ_f required for material crack propagation meets the following criteria (Suppl. Fig. 1):

$$\sigma \geq \sigma_f = \sqrt{\frac{2E\gamma_s}{\pi a}} \tag{1}$$

Where σ is the tensile stress on the film, E is the elastic modulus of the material, γ_s is the surface energy of the material, a is the length of a single crack. Given the inevitability of defects in materials, as the film thickness increases, the crack length a correspondingly enlarges, and the associated minimum stress for crack propagation gradually diminishes. When the thickness of the film exceeds the critical value,

the material undergoes spontaneous fracturing (Fig. 2e). In the fabrication of thin films utilizing traditional methodologies, the frequent observation of extensive cracking indicates that the film materials cannot be used (Fig. 2f).

For traditional film drying systems, the film itself is affected by liquid evaporation and organic matter decomposition, resulting in an overall compressive stress on the film. While the substrate induces tensile stress on the edges of the film, aligning with the basic conditions of the Griffith theory of fracture. Since the in-plane tensile stress is imparted by the substrate material, is it possible to fabricate dense film materials without relying on a substrate? We observed that when two solid interfaces are sufficiently close, the liquid can overcome gravity to suspend between the solids. This classic phenomenon is known as the capillary bridge, which is one of the few ways for liquids to suspend without substrates supporting on Earth. Inspired by this, we designed a simple grid composed of the hydrophilic resin that allows the liquid to be confined within the grid for the following processing to achieve a stress-eliminated fabrication, which we called SELF method (Fig. 2h).

During the initial drying phase of the liquid bridge (below 100 °C), as water and organic solvents evaporate, the liquid bridge gradually contracts and solidifies, forming a self-supported gel or an amorphous solid film (Fig. 2h). As the temperature rises, the grid material undergoes thermal decomposition, detaching from the capillary bridge film, and fully releasing the stress applied to the capillary bridge (Fig. 2i, j). The detachment of the edge of the film indicates the external tensile stress $\sigma = 0$, which is much smaller than the minimum crack stress σ_f. Thus, the requirements of the crack nucleation and propagation can no longer be met, preventing further growth of microcracks within the material (Fig. 2k). Since the film does not contact the substrate, there will be no tensile stress on the film. The resin network that supports the film material detaches from the film at a certain temperature (≈350 °C), allowing the film to undergo spontaneous shrinkage during drying and sintering without being affected by external forces. As a result, the microcracks within the material cannot receive sufficient energy to grow and propagate. However, due to factors such as gravity and air turbulence, liquid capillary bridges cannot always remain stable. When the liquid bridge film is too thin, it is easily disrupted by air impurities and turbulence. When the liquid bridge film is thick, external factors are less likely to cause the liquid bridge to break, making it easier to dry and form a complete solid (Fig. 2l). The capillary films derived from SELF method usually retain their integrity and cracks are rare to detect (Fig. 2m).

To elucidate the effect of mismatch stress on damage progression within ceramic films, a computational analysis was conducted employing a phase-field model[21,22]. This model shows the onset and advancement of cracks in the ceramic film by stimulating the expansion of the heated substrate or resin frame through equivalent displacement (Suppl. Fig. 2). We compared the damage evolution and showed the contours of the damage field of the conventional fabrication system (Fig. 2g) and the SELF system (Fig. 2n). The phase field, indicative of damage severity, is quantified on a scale from zero (intact) to one (completely damaged). The findings reveal that in the conventional system, multiple cracks develop as a consequence of tensile stress arising from the mismatch stress and the extensive adhesion between film and substrate. Conversely, in the SELF system, cracking is predominantly confined to the edge of the interface between the resin and film, attributed to localized stress concentration and limited bonding area. To further compare the cracking behavior of colloidal films with the same thickness during the drying and heating processes supported by conventional substrates, we wet the same grids with PZT colloidal precursor (Suppl. Fig. 3). One sample is contacted with a silicon wafer surface, and the other using the SELF method for comparison on the side. As the temperature slowly rises from room temperature to 300 °C, the gel film in contact with the silicon wafer first developed cracks, which gradually expanded, eventually forming large pores. The SEM results further investigate the crack situation of the film (Suppl. Fig. 4). Meanwhile, even if the grids of the SELF sample undergo significant deformation at high temperatures, the gel films remain dense and intact (Suppl. Movie 1), indicating that the SELF method effectively overcomes the limitations of critical crack thickness.

Analysis of film formation

In the SELF methodology, the construction of films is fundamentally based on the formation and stable existence of capillary liquid films on grids. Therefore, we need to investigate the forming conditions of capillary films in practical scenarios. Since the formation of the capillary film determines the final shaping of the PZT thick film, we use the filling ratio α (the fraction of the liquid capillary film formed on the grids) of the capillary film as an indicator to explore the success rate of the SELF method (Fig. 3a). Based on our experiment results (200 samples for each parameter), we divided the filling ratio into three phases based on the numerical range. When $\alpha > 80\%$, it is classified as phase I. At this stage, almost all the grids can form liquid films, resulting in the highest success rate and suitability for high-throughput production. When $20\% < \alpha < 80\%$, it is classified as phase II. At this stage, the probability of film formation is relatively high, suitable for most production needs. When $\alpha < 20\%$, it is classified as phase III. At this stage, the success rate of the film formation is low, requiring further adjustment of solution concentration, grid parameters, and other factors to improve the success rate. At small volume fractions, the liquid will wet the corners of the grid to minimize the surface energy. The angle formed between the meniscus of the liquid and the edge of the grid is governed by the contact angle (CA). If the CA > 90°, where the interface presents hydrophobic behavior, the liquid will be entirely precluded from filling the grid. As the liquid volume fraction increases, certain grids will be entirely occupied, culminating in the complete saturation of all grids.

Based on the aspiration to obtain large-area, scalable, and highly uniform materials, during our experiment, we submerge the grids directly into the precursor liquid to ensure comprehensive filling. However, influenced by external factors such as gravitational pull and air circulation, as well as internal determinants like solution concentration, the CA, and even the shrinkage ratio during the drying processes, the capillary bridges cannot fully occupy the grids with arbitrary dimensions (Fig. 3b). Given the challenges in modulating external variables, our research predominantly focusses on elucidating the intrinsic connection between the liquid properties and the results of the film formation. We first assess the relationship between the CA of the PZT sol-gel solution utilized in this experiment and the resin of the employed grid. The critical concentration of the PZT colloidal precursor solution is 4.89 mM, corresponding to a CA = 30°. Upon diluting the solution with acetic acid, the CA decreases with the solution concentration (Fig. 3c).

The filling ratio α and the survival rate β determine the success rate of fabricating films, where α is defined as the ratio of the number of capillary films on the grids after extracted from the precursor liquid to the total grids number of the grids, and β is defined as the ratio of the remaining gel films at the end of the drying process to the initial capillary liquid films. We employ grids with unit square sizes of 1, 1.5, 2, 2.5, and 3 mm, respectively, and submerge them in the precursor solutions with CA of 14°, 17°, 22°, 25°, 28°, and 30° to calculate the filling ratio and survival rate (Suppl. Fig. 5).

In general, as the grid size decreases, the force required to oppose the gravitational force of the capillary film also reduces, making film formation more feasible. The existing studies suggest that higher CA facilitates the formation of capillary films, which is not completely valid in this study. The low concentration of the precursor solution implies insufficient solute to sustain the stability of the capillary film during the drying process, leading to its rupture. Taking the grids with

https://doi.org/10.1038/s41467-024-54412-w

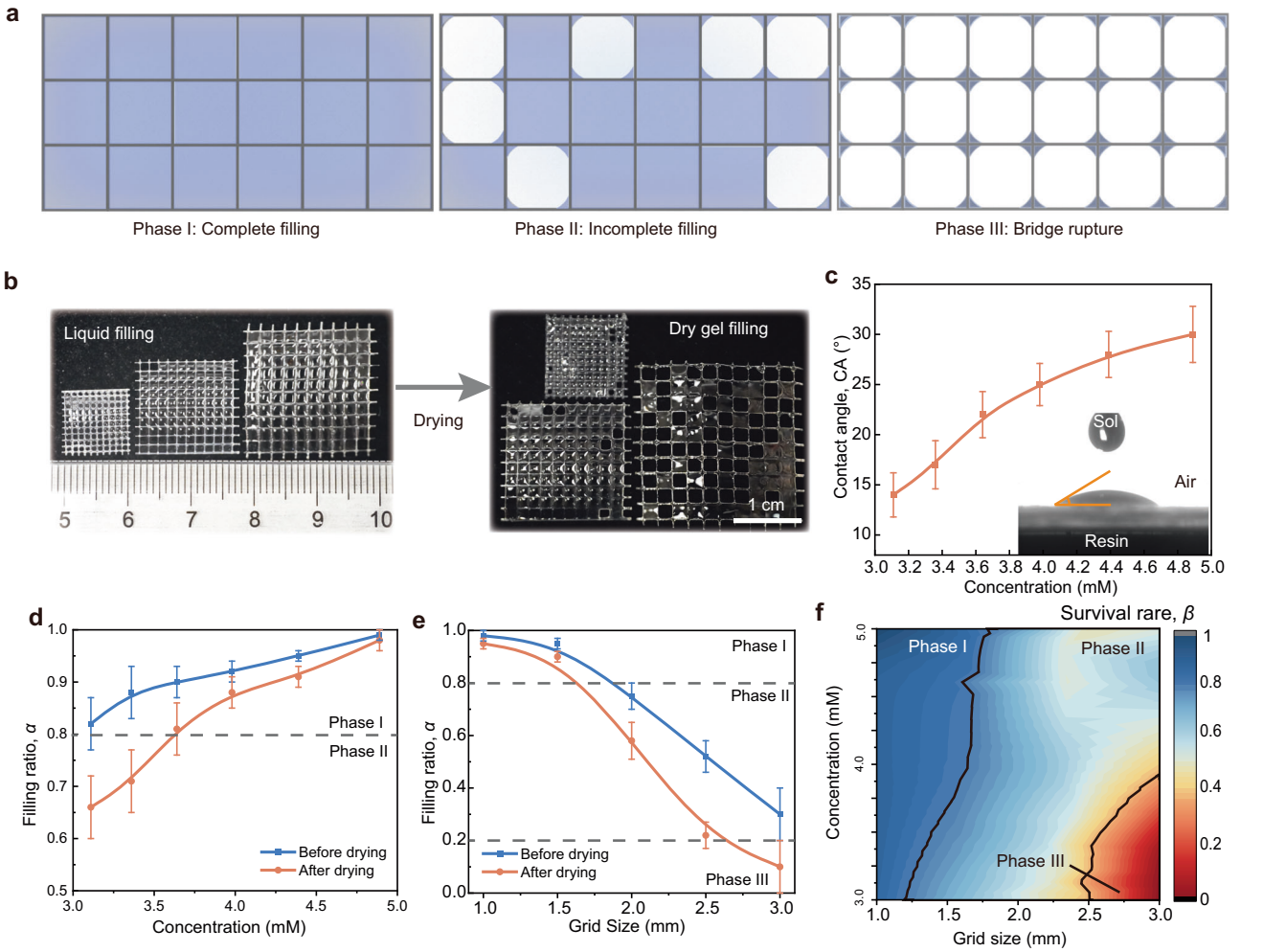

Fig. 3 | Formation of the capillary films. a The three main situations of the liquid PZT precursor filling in the grids. **b** The photographic of the sample with liquid filling and the gel film filling after drying. **c** The relationship between the CA and the PZT concentration. Error bars are standard deviations and include 10 independent measurements for each precursor concentration. **d** The filling ratio α results of the dried grids with a single square size of 1.5 mm. **e** The filling ratio α results as the function of the square size using the liquid with 4.89 mM. Error bars for (**d**–**e**) are standard deviations and include 200 independent measurements for each grid size. **f** The survival rate β results plotted by the isopleth diagram. Source data are provided as a Source Data file.

a unit square size of 1.5 mm as an example, almost all concentrations of the precursor solution exhibit a filling ratio exceeding 80%. However, after the drying process, the filling ratio for capillary films with lower concentration shows a significant decline (Fig. 3d), which is also consistent with the grids with any sizes (Fig. 3e). As the drying progresses, certain segments of the liquid capillary films tend to break, causing the liquid to reallocate to nearby films to reduce surface energy. The survival rate is plotted by the isopleth diagram (Fig. 3f). The trend indicates that smaller unit square sizes result in an augmented survival percentage of the capillary films.

Fabrication capability of the SELF strategy

To validate the feasibility of the SELF technique, we prepare PZT thick films via colloidal precursors. In traditional methods, the precise control of the concentration of the precursor for a single layer is essential to obtain crack-free films. Contrary to the conventional sol-gel techniques that demand as low a solution concentration as possible (<0.5 M), we prepared PZT colloidal precursor solution with a much higher concentration (2.5 M) for using in SELF technique. Under the influence of gravity, the adhesive force between the capillary film and the grid walls may be insufficient to counteract gravitational pull when the individual grid area is too large. Consequently, there is a limit to the size of each film segment. To overcome this limitation, we utilize 3D printing technology to fabricate grids composed of numerous arrays. This approach enables the production of large-area ceramic films by distributing the weight and gravitational forces across multiple smaller, manageable sections. Although achieving uniform thickness in capillary films presents a challenge, it is possible to modulate the thickness distribution by optimizing the solution concentration and drying conditions. Employing high-concentration precursor solutions can reduce the discrepancy between the thickest and thinnest points to less than 10% (Suppl. Fig. 6a). In contrast, using low-concentration solutions may result in a thickness variation exceeding 90% (Suppl. Fig. 6b).

The morphology of the film is intrinsically governed by the architectural specifications of the grids structure (Fig. 4a). For PZT films in this work, we can design and fabricate diverse topological configurations, including triangles, rectangles, and hexagons, as long as the dimension of the unit grid remains constrained below a threshold of 3 mm (Fig. 4b). The surface morphology is examined via the optical microscope with backlight to show the potential cracks more clearly. Furthermore, through design and optimization of the distributions of the grids with different sizes, the colloidal solution can confine itself exclusively to our predefined pathways, facilitating a tailored arrangement of the film materials, such as the word “HELLO” and the picture of a bear (Fig. 4b).

https://doi.org/10.1038/s41467-024-54412-w

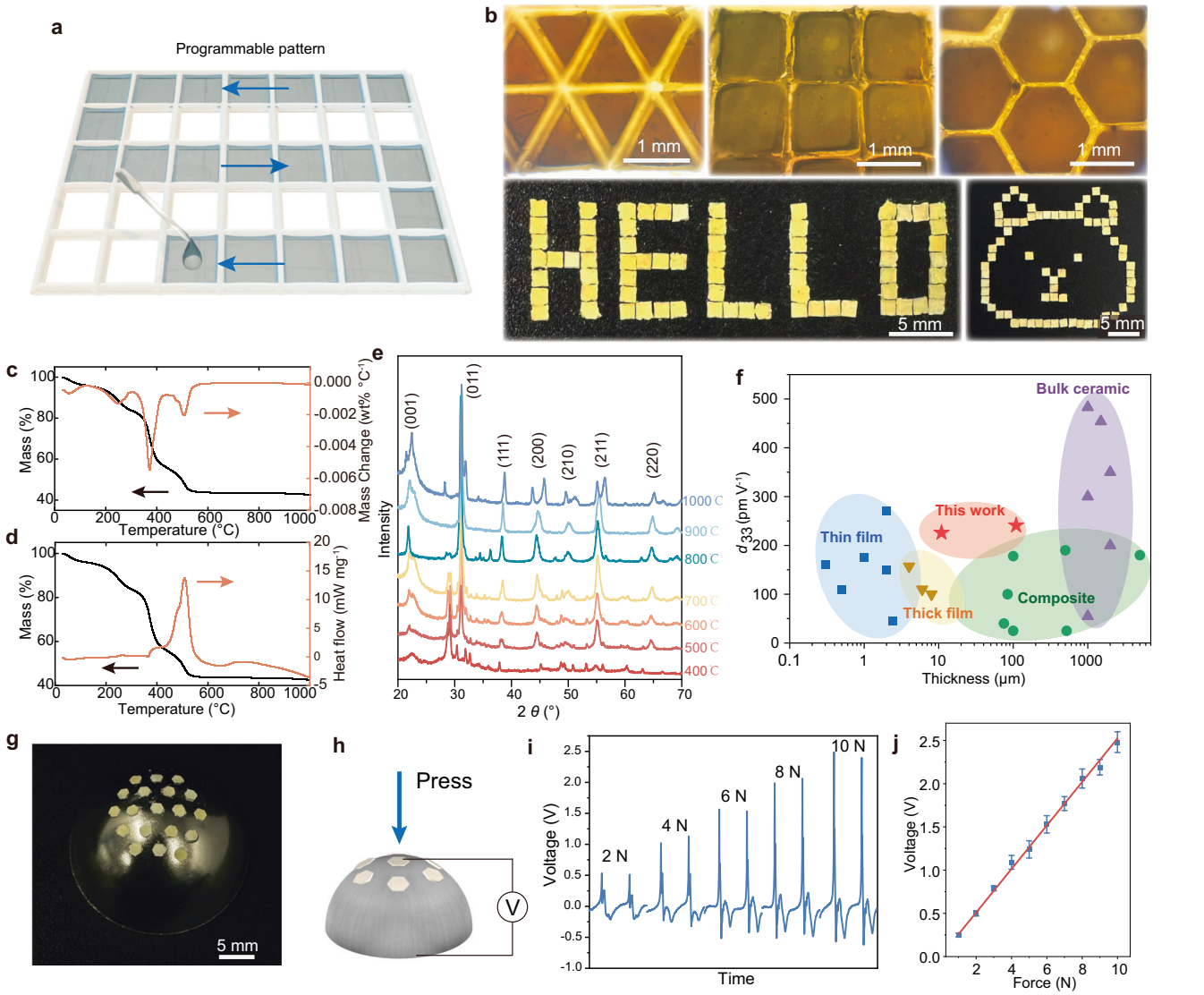

Fig. 4 | The processing capability. a The schematic illustration of the programmable film fabrication. **b** The 2D patterns derived from SELF method, including triangle grids, rectangular grids, hexagonal grids, "HELLO" pattern, and a bear pattern. **c** The simultaneous TGA and (**d**) DSC illustrate how the PZT colloidal film changes from liquid phase to solid crystals. **e** The XRD spectroscopy illustrates the crystallization process of PZT film under different temperatures. **f** Comparison of piezoelectric coefficient d_{33} of PZT-based materials prepared by various techniques with this work as a function of the material thickness[1,5,19,27–45]. **g** The assembled spherical 3D piezoelectric force sensor based on SELF-derived hexagonal PZT arrays. The photograph of the transferred PZT arrays on the spherical surface. **h** The working principle of the spherical piezoelectric sensor. **i** The detected signal from the sensor. **j** The linear fitting from the derived signal. Error bars are standard deviations and include 100 independent measurements at each force. Source data are provided as a Source Data file.

Combined TGA and differential scanning calorimetry (DSC) in the atmosphere can identify the phase transition of our material to take place between 220 and 550 °C (Fig. 4c, d). The PZT colloidal film undergoes a total mass loss of ≈58%, with three derivative peaks at 250, 370, and 510 °C that correlate with three endothermic peaks of the heat flow data. Each observed peak aligns with a sequence of three distinct reactive phases. In the initial two phases, the reactions involve the creation of peroxide groups, subsequently leading to a random chain cleavage and the release of various species, including water, carbon dioxide, hydrocarbons, and more substantial species. During this primary phase, CO_2 and H_2O emissions co-exist with the release of other species. The subsequent phase keeps this decomposition, but without the emergence of any additional high-mass species. During the final phase, the emissions of CO_2 and H_2O disappear gradually, followed by a series of crystallization processes in the film. According to the results, PZT precursor loses weight faster than the resin under 400 °C. Based on our observation, the separation of the PZT colloidal films and the grids origins from 350 °C. The weight of resin is quickly reduced until all the resins are decomposed when the temperature is larger than 400 °C (Suppl. Fig. 7), while the weight of PZT will retain at 42%. Therefore, the shrinkage of the PZT precursor plays a more important role under 400 °C to create the crack along the interface between the films and the grids. When the temperature is larger than 400 °C, the decomposition of the resin will result in the propagation of the cracks until the materials are totally separated.

The crystallization process of the PZT film is investigated via X-ray diffraction (Fig. 4e). Under 500 °C, an initial perovskite phase emerges, accompanied by a number of secondary phases, suggesting partial sintering. Between 600 and 800 °C, the perovskite phase is essentially formed, but there are still minor extraneous peaks, which are detrimental to the performance of piezoelectric materials. When the sintering temperature exceeds 800 °C, the crystal is gradually crystallized. The Raman spectroscopy further examined the crystallinity of the PZT film (Suppl. Fig. 8). We further examined the surface

morphology of PZT films with different sintering temperatures under SEM (Suppl. Fig. 9). When the sintering temperature is larger than 1000 °C, grains will be too large, and the porosity is increased. Conversely, at temperatures below 800 °C, the ceramic crystallization is incomplete. Therefore, in this study, the PZT films used for piezoelectric properties measurement and device fabrication are sintered at 900 °C.

The piezoelectric property is measured via quasi-static d_{33} meter (Suppl. Fig. 10). The average d_{33} value is about 229 pC V^{-1}, which is comparable to that of un-doped PZT ceramics (Fig. 4f). Therefore, the proposed SELF process can prepare films in a wide range of thicknesses while considering of high-quality crystals and electric properties, which eliminates the processing barrier between thin films to thick or even bulk ceramics without sacrificing on performances.

For the commonly used piezoelectric array devices, it has been observed that as the decreasing size of individual units, the likelihood of extensive crack propagation increases, especially during cutting or dicing. This occurrence can significantly compromise the performance of the device, leading to possible operational inefficiencies or even complete malfunction. Utilizing the SELF technique offers an effective solution to address the challenges associated with cutting, enabling the attainment of the desired array configurations simply by tailoring the grid layout. Furthermore, owing to the intrinsic freestanding nature of the film materials prepared via the SELF method, we can readily transfer the fabricated films to any substrate or surface with varied geometries. For instance, the derived PZT films can be transferred onto the spherical surface to construct a conformal PZT array (Fig. 4g). By integrating electrodes (silver paste at the bottom and Ag film sputtered at the top) on the PZT surface, we developed a spherical piezoelectric sensor (Fig. 4h–j). When a force ranging from 0 to 10 N is applied to the device, an open-circuit voltage output between 0 and 2.5 V is observed. By fitting the data of the output voltage to the input force, it is evident that the piezoelectric force sensor exhibits excellent linearity.

Application in ultrasound focusing transmitter

Ultrasound-focusing technology realizes efficient and precise energy transfer by concentrating ultrasonic waves in targeted areas, thereby finding extensive applications in non-invasive medical imaging, tumor ablation, and non-destructive testing. Traditional focused ultrasound transmitters primarily utilize piezoelectric ceramic arrays and curved piezoelectric ceramics to achieve focusing effects[2,23]. However, array-type piezoelectric ceramics involve precise cutting processes that may lead to material loss and increased costs. Curved ceramics often require complex fabrication processes and are typically characterized by large volume and thickness, resulting in lower frequency response. Here, we explore the rapid preparation of piezoelectric thick-film arrays using the SELF method, which naturally results in films with concave shapes that endow thicker edges and thinner centers. We processed these PZT films into ultrasound transmitters that produce focused ultrasound fields.

To demonstrate the unidirectional focused ultrasound transmitter, we utilize the traditional polishing method to flatten one side of the film (Supplementary Note 2, Suppl. Figs. 11 and 12). Through a series of processes, including electrode deposition and resin encapsulation, we fabricated a single focused ultrasound transmitter unit (Fig. 5a). The specific fabrication methods are described in detail in the Methods section.

The experiment is conducted inside a water tank (Fig. 5b). When the emitter generates ultrasonic waves, the hydrophone records the sound pressure amplitude along the acoustic axis, moving in increments of 0.1 mm. Numerical simulations indicate that an energy spot appears at a distance of 5–7 mm from the transmitter (Fig. 5c). The impedance curve of the piezoelectric device is measured using a network analyzer, revealing a thickness mode resonance frequency of 20 MHz (Fig. 5d). To exhibit the universality of the ultrasonic transmitter, we choose a commonly used frequency of 1 MHz, which differs from the device's resonance frequency. We find that at 6.2 mm, the sound pressure is significantly higher than that at other positions, which is consistent with the simulation results (Fig. 5d–f). This result indicates that the concave mirror-shaped piezoelectric ceramic film produced via SELF method has a high resonance frequency and is inherently suited for ultrasonic applications.

Discussion

We introduce the stress-eliminated liquid-phase fabrication method, elucidating its intrinsic merits in preventing the formation of cracks in thin films during the drying process. We fabricate PZT ceramic films as a paradigm to exhibit the advantages of this technique. The results show that PZT films with diameters ranging from 0 to 3 mm and thicknesses from 1 to 100 μm are easily derived via this method. The observed d_{33} value of PZT reached 229 pC V^{-1}, which closely parallels the performance of bulk ceramics. Additionally, we delved into the optimal conditions for film formation via the SELF method, determining that higher concentrations and smaller grid sizes facilitate material preparation. We further attempt to craft diverse grid geometries and various grids with distinct wettability pathways to show the programming capability of the SELF method.

However, the gravity forces coupled with the surface tension of the liquid render it challenging to stabilize films in grids exceeding 3 mm. Consequently, the dimensions of individual films are inherently restricted. Augmenting the fabrication scale necessitates a massive array deployment. Potential avenues to address these limitations could be surface tension optimization of the materials and the utilization of external stimulations to counteract the influence of gravity, thereby enlarging the individual film scale to adapt to diverse application scenarios. Furthermore, the SELF method can also be used for nanoscale material processing by using smaller grids, avoiding complicated steps like photolithography and dicing, which significantly increase the fabrication cost and difficulty.

In the SELF method, materials form within individual grids without the interference of a substrate. This aspect allows the easy integration of the films with other materials and systems, paving the way for the construction of electronic components and 3D devices. Interestingly, filling grids with a liquid precursor that subsequently reacts to form a film resembles the behavior of biomolecular condensates. This suggests that the materials fabrication is not the only application of the SELF method. By employing different liquid compositions in neighboring grids, the method offers a platform for extensive investigation into various biological and chemical processes, presenting significant application potential in disciplines like biology, materials science, and chemistry.

Methods

Materials preparation

Preparation of grids frameworks. The topologies of a single grid of the grid framework are carefully designed. The grids are produced via commercial stereolithography 3D printing (JC-M10, JANSUM) with the commercial resin JC-H-00, which mainly contains polyurethane acrylate, cyclic trimethylolpropane formal acrylate (CTFA), and 1,3,5-trimethylcyclohexyl acrylate. The grids are printed with 25 μm layers. The grids are required to be rinsed by isopropyl alcohol twice and a post-curing process by exposing them to 405 nm light before use.

Preparation of PZT [$Pb(Zr_{0.52}TiO_{.48})O_3$] sol solution. The $Pb(Zr_{0.52}Ti0_{.48})O_3$ solution contains Pb 10% excess to compensate for the volatilization of PbO in high temperatures during the annealing process. Lead (II) acetate trihydrate ($Pb(CH_3COOH_2) \cdot 3H_2O$ (TCI) with 6.8 g is firstly dissolved in 3 mL acetic acid (Alfa Aesar, 99%) in 90 °C for 1 h and mixed by magnetic stirring. When it is completely dissolved, cool down the solution to room temperature. Zirconium (IV) *n*-

https://doi.org/10.1038/s41467-024-54412-w

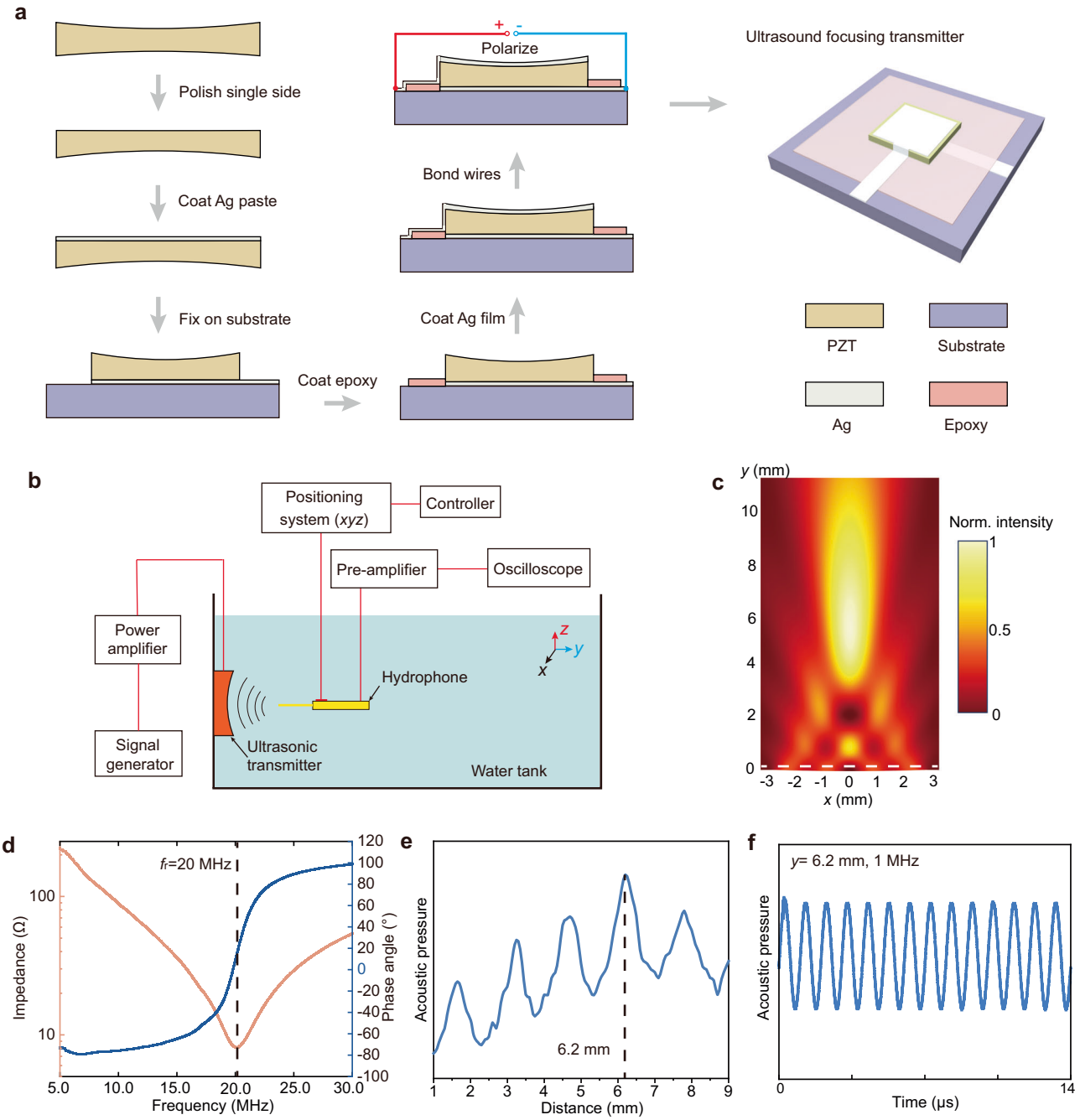

Fig. 5 | The ultrasound focusing transmitter fabricated based on the SELF-derived PZT films. a The processing and fabrication flow of the ultrasound transmitter. **b** The set up of the ultrasound focusing transmitter experiment. **c** The simulation result of the acoustic intensity distribution of the ultrasound transmitter. **d** The resonance frequency at the thickness mode of the device. **e** The recorded acoustic pressure along the acoustic axis. **f** The recorded wave at $y = 6.2$ mm by the hydrophone. Source data are provided as a Source Data file.

propoxide ($C_{12}H_{28}O_4Zr$, TCI, 70 wt.% in 1-proponol) with 3.45 g is mixed with 2.45 g titanium (IV) butoxide ($C_{16}H_{36}O_4Ti$, TCI, 99%) in another container. Then zirconium (IV) *n*-propoxide and titanium (IV) butoxide are added to lead (II) acetate trihydrate the solution, and heat up to 90 °C with stirring for 6 h in atmosphere. The as-prepared solution will be stored in the atmosphere at least three days for aging. Finally, a transparent and pale yellow PZT sol is obtained.

PZT films fabrication via SELF method. The prepared liquid solution is first poured into a glass dish. Then, the 3D-printed grid framework is carefully immersed into the solution. After ensuring that all the grids are fully wetted, slowly lift the grid out of the solution, allowing the solution to evenly suspend between the grid's interstices. The sample is then placed on a heating platform and dried at 60 °C. When the liquid capillary bridges transition from to the gel state, the sample can be carried directly into a muffle furnace for sintering. After cooling with air, the PZT film array can be retrieved.

Characterization

Materials characterization. The surface morphologies are examined via an optical electron microscope (AOSVI, AF516C) and a scanning electron microscope (SEM, FEI Quanta 450). The crystal structure is characterized by X-ray diffraction (XRD, Rigaku SmartLab). The Raman spectrum is characterized by a Raman spectrometer (Perkinelmer

Raman station 400 F). The DSC and thermogravimetric (TG) curves are conducted by a thermogravimetric analyzer (TGA/DSC 3+, METTLER TOLEDO). The CA are measured by Standard Contact Angle Goniometer (OCA25, Dataphysics). The voltage output is collected via an oscilloscope (Rohde & Schwarz RTE1024).

Piezoelectric measurement

PZT film materials are first coated with 100 nm silver electrodes on the top and bottom sides using magnetron sputtering, and then the PZT film is fixed onto a conductive substrate (here: stainless steel). The films are then heated in an oil bath to 120 °C, and a DC electric field of 50 kV cm^{-1} is applied. After polarizing for 1 h, the oil bath is cooled to room temperature, and the DC power supply is turned off, completing the polarization process. Before performing PFM testing, the PZT samples are left at room temperature for 24 h to avoid the influence of surface charges and other factors. The d_{33} value of the PZT films is measured by the quasi-static d_{33} meter (YE2730A, SINOCERA). The resonance frequency and the phase angle are measured via the ENA network analyzer (E5061B, Keysight).

Simulations

Phase-field method analysis. The phase-field method is used to study the fracture behavior of the ceramic film in the colloidal-substrate system and the single grid system (detailed information in Supplementary Note 1). The analysis is implemented into the general software package ABAQUS as a UEL (user-defined element). It is required to utilize the theory of linear elastic fracture energy variation as well as the specific form of crack regularization for the brittle material[24]. The PF-CZM constitutive model and Miehe strain energy split method have been assigned to the ceramic film with 10 μm thickness using plane strain elements[25]. An efficient and robust staggered scheme is adopted, decoupling the fracturing phase and displacement field. In the actual preparation process, mismatch stress originates from the chemical shrinkage and solidification of ceramic film and the thermal expansion of Si Substrate or resin grid[26]. To simplify the analysis, an equivalent 4% strain by displacement control was applied to Si Substrate or resin grid to study crack propagation without considering thermal effects and chemical process. The monotonic tensile loading and the boundary condition were then imposed on the model. The length scale parameter is set as 1 μm, which should be four times above the element size to ensure the accuracy of crack prediction. The damage phase field from zero (undamaged) to one (fully damaged) on the ceramic film in the colloidal-substrate system and Single Grid are presented in this research.

Acoustic field simulations

We employed COMSOL Multiphysics 6.1 to simulate ultrasound propagation and sound field distribution in water, serving as a mutual validation for experimental outcomes. Ultrasound waves originated from a slightly curved surface modeled as a circular arc in a two-dimensional simulation, incorporating geometric details of the piezoelectric thin film. The arc span matched the film's edge length of 6 mm, with a sagitta of 0.05 mm and a radius of 90 mm. We utilized the Pressure Acoustics, Frequency Domain module to induce oscillation of the arc at 1 MHz, projecting sound waves into a water domain (7 mm × 11.5 mm) bordered by a Perfectly Matched Layer to prevent wave reflections. To maintain simulation accuracy, the maximum mesh size was kept below one-seventh of the ultrasonic wavelength. The resulting intensity diagram showed sound waves concentrating along the acoustic axis and forming an energy spot between 5 and 6.5 mm from the source, aligning well with the experimental data.

Device manufacturing

Conformal sensor arrays. The magnetron sputtering (Q150TS, Quorum) is used to coat a 100 nm thick silver conductive film on both the upper and lower surfaces of the PZT film. Next, the film is fixed onto a stainless steel shell using silver paste. We designed a serpentine electrode array to make physical contact with the PZT film and used thermoplastic polyurethane encapsulation to secure the structure, resulting in a spherical mechanical sensor.

Ultrasound focusing transmitter

One side of the film is polished to obtain a flat surface, and then a 100 nm thick silver conductive film is deposited on it via magnetron sputtering (Fig. 5a). Simultaneously, we fabricate a $10 \times 10 \times 2\ mm^3$ planar substrate via 3D printing, adhere the planar side of the piezoelectric film to the substrate pre-coated with electrodes, and fix it using epoxy. After the epoxy fully cures, the top surface of the PZT is also coated with a 100 nm thick silver film via magnetron sputtering, and the conductive path is connected to the substrate to facilitate external wiring. The sound pressure is measured by a hydrophone (NH1000, Precision Acoustics).

Data availability

The data that support the findings of this study are available from the corresponding authors upon request. Source data are provided with this paper.

References

1. Yang, A., Wang, C.-A., Guo, R., Huang, Y. & Nan, C.-W. Effects of sintering behavior on microstructure and piezoelectric properties of porous PZT ceramics. *Ceram. Int.* **36**, 549–554 (2010).
2. Fei, C. et al. PMN-PT single crystal ultrasonic transducer with half-concave geometric design for IVUS imaging. *IEEE Trans. Biomed. Eng.* **65**, 2087–2092 (2018).
3. Singh, K. B. & Tirumkudulu, M. S. Cracking in drying colloidal films. *Phys. Rev. Lett.* **98**, 218302 (2007).
4. Li, X. et al. Evaporation-induced sintering of liquid metal droplets with biological nanofibrils for flexible conductivity and responsive actuation. *Nat. Commun.* **10**, 3514 (2019).
5. Balma, D. et al. High piezoelectric longitudinal coefficients in sol–gel PZT thin film multilayers. *J. Am. Ceram. Soc.* **97**, 2069–2075 (2014).
6. Ding, J. et al. An arrayed giant electrorheological fluid damper with energy harvesting and tunable-damping capacity. *IEEE/ASME Trans. Mechatronics* 1–10 (2024).
7. Lama, H., Gogoi, T., Basavaraj, M. G., Pauchard, L. & Satapathy, D. K. Synergy between the crack pattern and substrate elasticity in colloidal deposits. *Phys. Rev. E* **103**, 32602 (2021).
8. Lee, Y. et al. Cracking of colloidal films to generate rectangular fragments. *Langmuir* **38**, 4935–4941 (2022).
9. Bourrianne, P. et al. Crack morphologies in drying suspension drops. *Soft Matter* **17**, 8832–8837 (2021).
10. Griffith, A. A. & Taylor, G. I. VI The phenomena of rupture and flow in solids. *Philos. Trans. R. Soc. Lond. Ser. A* **221**, 163–198 (1997).
11. Santanach Carreras, E., Chabert, F., Dunstan, D. E. & Franks, G. V. Avoiding "mud" cracks during drying of thin films from aqueous colloidal suspensions. *J. Colloid Interface Sci.* **313**, 160–168 (2007).
12. Lee, S.-Y. et al. Selective crack suppression during deformation in metal films on polymer substrates using electron beam irradiation. *Nat. Commun.* **10**, 4454 (2019).
13. Jiang, L. et al. Flexible ultrasound-induced retinal stimulating piezo-arrays for biomimetic visual prostheses. *Nat. Commun.* **13**, 3853 (2022).
14. Du, W. et al. Conformable ultrasound breast patch for deep tissue scanning and imaging. *Sci. Adv.* **9**, eadh5325 (2024).
15. Pursiainen, O. L. J. et al. Shear-induced organization in flexible polymer opals. *Adv. Mater.* **20**, 1484–1487 (2008).
16. Hagan, E. W. S., Charalambides, M. N., Young, C. R. T., Learner, T. J. S. & Hackney, S. Viscoelastic properties of latex paint films in

tension: Influence of the inorganic phase and surfactants. *Prog. Org. Coat.* **69**, 73–81 (2010).
17. Cai, Z. et al. From colloidal particles to photonic crystals: advances in self-assembly and their emerging applications. *Chem. Soc. Rev.* **50**, 5898–5951 (2021).
18. Wang, D. et al. Fabrication of bimorph lead zirconate titanate thick films on metal substrates via the cold sintering-assisted process. *Acta Mater.* **195**, 482–490 (2020).
19. Peddigari, M. et al. Giant energy density via mechanically tailored relaxor ferroelectric behavior of PZT Thick Film. *Adv. Mater.* **35**, 2302554 (2023).
20. Zheng, Q. et al. Thin ceramic PZT dual- and multi-frequency pMUT arrays for photoacoustic imaging. *Microsyst. Nanoeng.* **8**, 122 (2022).
21. Nazeer, H., Nguyen, M. D., Rijnders, G., Abelmann, L. & Sardan Sukas, Ö. Residual stress and Young's modulus of pulsed laser deposited PZT thin films: Effect of thin film composition and crystal direction of Si cantilevers. *Microelectron. Eng.* **161**, 56–62 (2016).
22. Xu, J., Xie, S., Xu, Q., Wang, Q. & Chen, Y. Crack propagation behavior in lead zirconate titanate-based ferroelectric ceramics. *Ceram. Int.* **46**, 12430–12436 (2020).
23. Jian, X. et al. Development of self-focusing piezoelectric composite ultrasound transducer using laser engraving technology. *IEEE Trans. Ultrason. Ferroelectr. Freq. Control* **66**, 1866–1873 (2019).
24. Bourdin, B., Francfort, G. A. & Marigo, J.-J. The variational approach to fracture. *J. Elast.* **91**, 5–148 (2008).
25. Wu, J.-Y. et al. Chapter one - phase-field modeling of fracture. In: (eds. Bordas, S. P. A. & Balint, D. S. B. T.-A. in A. M.) vol. 53 1–183 (Elsevier, 2020).
26. Gerasimov, T. & De Lorenzis, L. On penalization in variational phase-field models of brittle fracture. *Comput. Methods Appl. Mech. Eng.* **354**, 990–1026 (2019).
27. Hong, Y. et al. Hierarchically interconnected piezoceramic textile with a balanced performance in piezoelectricity, flexibility, toughness, and air permeability. *Adv. Funct. Mater.* **31**, 2104737 (2021).
28. Guler, Z., Vazquez, I. R. & Jackson, N. Multi-functional 0–3 composite polyimide films for microsystem applications. *Smart Mater. Struct.* **32**, 75015 (2023).
29. Almusallam, A. et al. Development of a low temperature PZT/polymer paste for screen printed flexible electronics applications. in *Sensors, 2014 IEEE* 2183–2186 (2014).
30. Eichhorn, F. et al. Influence of cell size on mechanical and piezoelectric properties of PZT and LNKN ceramic foams. *Adv. Eng. Mater.* **19**, 1700420 (2017).
31. Jiang, X. N., Sun, C., Zhang, X., Xu, B. & Ye, Y. H. Micro-stereolithography of lead zirconate titanate thick film on silicon substrate. *Sens. Actuat. A Phys.* **87**, 72–77 (2000).
32. Hong, Y. et al. A wood-templated unidirectional piezoceramic composite for transmuscular ultrasonic wireless power transfer. *Energy Environ. Sci.* **14**, 6574–6585 (2021).
33. Liu, Y. et al. Electronic skin from high-throughput fabrication of intrinsically stretchable lead zirconate titanate elastomer. *Research* **2020**, 1085417 (2020).
34. Guo, F. et al. Secondary phase softening effect in PZT-based ceramics by introducing the random electric fields. *J. Am. Ceram. Soc.* **106**, 5258–5268 (2023).
35. Boucher, E., Guyomar, D., Lebrun, L., Guiffard, B. & Grange, G. Effect of (Mn, F) and (Mg, F) co-doping on dielectric and piezoelectric properties of lead zirconate titanate ceramics. *J. Appl. Phys.* **92**, 5437–5442 (2002).
36. Karapuzha, A. S., James, N. K., Khanbareh, H., van der Zwaag, S. & Groen, W. A. Structure, dielectric and piezoelectric properties of donor doped PZT ceramics across the phase diagram. *Ferroelectrics* **504**, 160–171 (2016).
37. Kalem, V., Çam, İ. & Timuçin, M. Dielectric and piezoelectric properties of PZT ceramics doped with strontium and lanthanum. *Ceram. Int.* **37**, 1265–1275 (2011).
38. Ramam, K. & Lopez, M. Ferroelectric and piezoelectric properties of Ba modified lead zirconium titanate ceramics. *J. Phys. D. Appl. Phys.* **39**, 4466 (2006).
39. Vu, H. T. et al. Ferroelectric and piezoelectric responses of (110) and (001)-oriented epitaxial Pb(Zr0.52Ti0.48)O3 thin films on all-oxide layers buffered silicon. *Mater. Res. Bull.* **72**, 160–167 (2015).
40. Hu, B. et al. Piezoelectric properties of epitaxial Pb(Zr0.525, Ti0.475) O3 films on amorphous magnetic metal substrates. *J. Appl. Phys.* **111**, 07D916 (2012).
41. Keech, R. et al. Declamped piezoelectric coefficients in patterned 70/30 lead magnesium niobate–lead titanate thin films. *Adv. Funct. Mater.* **27**, 1605014 (2017).
42. Liu, S., Zou, D., Yu, X., Wang, Z. & Yang, Z. Transfer-free PZT thin films for flexible nanogenerators derived from a single-step modified sol-gel process on 2D mica. *ACS Appl. Mater. Interfaces* **12**, 54991–54999 (2020).
43. Liu, Y. et al. All-ceramic flexible piezoelectric energy harvester. *Adv. Funct. Mater.* **32**, 2209297 (2022).
44. Jung, J. et al. 31-mode piezoelectric micromachined ultrasonic transducer with PZT thick film by granule spraying in vacuum process. *Appl. Phys. Lett.* **110**, 212903 (2017).
45. Thiele, E. S., Damjanovic, D. & Setter, N. Processing and properties of screen-printed lead zirconate titanate piezoelectric thick films on electroded silicon. *J. Am. Ceram. Soc.* **84**, 2863–2868 (2001).

Acknowledgements

The work described in this paper was supported by the Hong Kong Research Grants Council (GRF Project Nos. 11212021 and 11210822, both received by Z.Y.).

Author contributions

S.L. and Z.Y. conceived the project and designed the studies. S.L., Y.H., W.H., and Y.Z. performed experiments and analyzed the experimental data. W.H., X.Z., and Y.Z. worked on simulation, with assistance from X.Y., X.L., Z.Z., X.Y., Y.S., W.L., and Z.P. in materials characterization. S.L., Y.H., W.H., and Y.Z., composed the manuscript. X.Y, Z.W., and Z.Y. reviewed and revised the manuscript. All authors discussed the results and commented on the manuscript. S.L., Y.H., W.H., and Y.Z. contributed equally to this study and shared the first authorship.

Competing interests

The authors declare no competing interests

Additional information

Supplementary information The online version contains supplementary material available at https://doi.org/10.1038/s41467-024-54412-w.

Correspondence and requests for materials should be addressed to Shiyuan Liu, Xi Yao, Zuankai Wang or Zhengbao Yang.

Peer review information *Nature Communications* thanks Hyunsik Yoon, Jungho Ryu, and the other, anonymous, reviewer(s) for their contribution to the peer review of this work. A peer review file is available.